

The Effects of Linear Matter Power Spectrum Enhancement on Dark Matter Substructure

ETHAN O. NADLER,¹ VERA GLUSCEVIC,² AND ANDREW BENSON³

¹*Department of Astronomy & Astrophysics, University of California, San Diego, La Jolla, CA 92093, USA*

²*Department of Physics & Astronomy, University of Southern California, Los Angeles, CA 90007, USA*

³*Carnegie Observatories, 813 Santa Barbara Street, Pasadena, CA 91101, USA*

ABSTRACT

We present cosmological dark matter (DM)–only zoom-in simulations of a Milky Way (MW) analog originating from enhanced linear matter power spectra $P(k)$ relative to the standard cold, collisionless DM (CDM) cosmology. We consider a Gaussian power excess in $P(k)$ followed by a cutoff in select cases; this behavior could arise from early-universe physics that alters the primordial matter power spectrum or DM physics in the radiation-dominated epoch. We find that enhanced initial conditions (ICs) lead to qualitative differences in substructure relative to CDM. In particular, the subhalo mass function (SHMF) resulting from ICs with both an enhancement and cutoff is amplified at high masses and suppressed at low masses, indicating that DM substructure is sensitive to features in $P(k)$. Critically, the amplitude and shape of the SHMF enhancement depend on the wave number of the $P(k)$ excess and the presence or absence of a cutoff on smaller scales. These alterations to the SHMF are mainly imprinted at infall rather than during tidal evolution. Additionally, subhalos are found systematically closer to the host center and their concentrations are increased in scenarios with $P(k)$ enhancement. Thus, nonlinear mode coupling must be captured to enable $P(k)$ reconstruction using DM substructure.

Keywords: Dark matter (353); *N*-body simulations (1083); Galaxy dark matter halos (1880)

1. INTRODUCTION

Dark matter (DM) substructure is a powerful cosmological probe. The initial conditions (ICs) that seed DM subhalo populations are captured by the linear matter power spectrum $P(k)$, where k is the wave number. Deviations in $P(k)$ from standard cold, collisionless DM (CDM) predictions on small scales can affect the mass function, density profiles, and redshift evolution of DM subhalo populations and the satellite galaxies they host (see Bechtol et al. 2022 for a review).

A wide range of physics can affect $P(k)$ on small scales. In particular, $P(k)$ depends on both the primordial matter power spectrum and its growth until recombination, captured by linear transfer functions. The primordial power spectrum is determined by the physics of inflation, while transfer functions capture the early expansion history and DM physics in the radiation-dominated epoch (for reviews, see Allahverdi et al. 2021; Arbey & Mahmoudi 2021; Achúcarro et al. 2022).

For example, many models beyond the CDM paradigm lead to a cutoff in $P(k)$ on sub-Mpc scales, which reduces the abundance of subhalos and satellite galaxies in the Milky Way (MW; Nadler et al. 2025a). On the other hand, the effects of $P(k)$ enhancement on subhalo populations are less well studied. More generally, understanding the mapping be-

tween features in $P(k)$ and DM subhalo populations is critical to enable tests of new physics using small-scale structure.

Structure formation in cosmologies with $P(k)$ enhancement is difficult to simulate once the relevant modes become nonlinear. In particular, unlike scenarios with a $P(k)$ cutoff, the growth of small-scale density perturbations is more difficult to capture accurately if there is substantial power on scales below the resolution limit of the simulation. Note that the dimensionless CDM power spectrum $k^3 P(k)$ grows logarithmically with increasing k ; even for such mild growth toward small scales, unresolved small-scale power can affect the properties of structure on larger scales. A classic effect of unresolved small-scale power is that the innermost regions of simulated CDM halos have constant-density cores due to limited resolution (Power et al. 2003). These artificial cores become smaller as resolution is increased and give way to a steep power law “prompt cusp” if the first generation of halo collapse is captured (Delos & White 2023). Because numerical disruption is accelerated in the presence of density profile cores (van den Bosch et al. 2018; Errani & Navarro 2021; Benson & Du 2022), unresolved small-scale power can thus impact the properties of subhalos that are nominally resolved.

Here, we study how subhalo populations respond to $P(k)$ enhancement using high-resolution simulations that accurately capture small-scale structure formation on scales relevant for MW satellites. As a benchmark example, we model $P(k)$ enhancement using a Gaussian excess that reaches $\approx 5\times$ the power in CDM at a chosen scale. Enhancement in the primordial power spectrum is a hallmark of many inflation-

ary models (e.g., with multiple fields or features in the inflaton potential; Adams et al. 2001; Palma et al. 2020) and can also arise from an early matter-dominated epoch, vector or axion DM, and primordial magnetic fields (e.g., Erickcek & Sigurdson 2011; Graham et al. 2016; Buschmann et al. 2020; Gorghetto et al. 2021; Pavičević et al. 2025). Enhanced ICs have garnered interest because they can increase halo and galaxy abundances and inner densities at high redshifts (Tkachev et al. 2024b; Eroshenko et al. 2024), potentially bringing simulation predictions into better agreement with JWST galaxy surveys, as compared to standard CDM (Tkachev et al. 2024a; Pilipenko et al. 2024). However, the consequences for subhalo populations are relatively unexplored. Understanding this interplay between $P(k)$ and subhalo population statistics will be necessary to interpret upcoming dwarf galaxy, stellar stream, and strong-lensing data in the context of early-universe and DM physics.

Building on the COZMIC simulations (Nadler et al. 2025a; An et al. 2025; Nadler et al. 2025b), we therefore run new zoom-in simulations of a MW analog to quantify how $P(k)$ enhancement impacts subhalo populations. In select cases, we also include cutoffs on scales smaller than the enhanced modes in $P(k)$ to mimic the effects of modeling these ICs with artificially-truncated small-scale power. Specifically, we run nine new high-resolution cosmological DM-only zoom-in simulations of a MW analog originally from the Milky Way-est suite (Buch et al. 2024) with $P(k)$ enhancement and/or suppression. This host was simulated with $P(k)$ suppression appropriate for warm, fuzzy, interacting, mixed, and self-interacting DM in the COZMIC suite (Nadler et al. 2025a; An et al. 2025; Nadler et al. 2025b).

Our simulation results provide a benchmark for constraining $P(k)$ enhancement using substructure and are relevant for probing a wide range of models with enhanced small-scale power, including cosmologies with a positive scalar spectral index running (e.g., Gilman et al. 2022; Esteban et al. 2024; Dekker et al. 2022). Substructure constraints on these models have mainly relied on semi-analytic predictions to connect $P(k)$ to subhalo populations. Calibrating such models on cosmological simulations that capture the full, nonlinear coupling of small-scale modes in the presence of modifications to $P(k)$, is therefore timely. The mapping from our Gaussian enhancement scenario to specific DM, inflation, and early-universe models will be addressed in future work.

This paper is organized as follows. In Section 2, we describe our simulations. In Section 3, we study the subhalo mass function (SHMF); in Section 4, we dissect these results by studying isolated versus subhalo mass functions, subhalo radial distributions, and the subhalo mass-concentration relation. We summarize and discuss our results in Section 5.

We use cosmological parameters $h = 0.7$, $\Omega_m = 0.286$, $\Omega_b = 0.049$, $\Omega_\Lambda = 0.714$, $\sigma_8 = 0.82$, and $n_s = 0.96$ (Hinshaw et al. 2013). Virial masses are defined via $\Delta_{\text{vir}} \approx 99 \times \rho_{\text{crit}}$, where ρ_{crit} is the critical density of the Universe at $z = 0$ (Bryan & Norman 1998). We refer to halos within the virial radius of our MW host as “subhalos,” and halos outside the virial radius of any larger halo as “isolated halos.”

2. SIMULATION OVERVIEW

2.1. Initial Conditions

We parameterize $P(k)$ for the Gaussian enhancement model as follows (Tkachev et al. 2024b)

$$\mathcal{T}_{\text{bump}}(k) \equiv \sqrt{\frac{P_{\text{bump}}(k)}{P_{\text{CDM}}(k)}} = 1 + A \exp \left[-\frac{(\log(k) - \log(k_0))^2}{\sigma_k^2} \right], \quad (1)$$

where $\mathcal{T}(k)$ is the transfer function and A , k_0 , and σ_k are free parameters. Throughout, we set $A = 2$ and $\sigma_k = 0.5$; we describe our method for choosing k_0 below.

We parameterize $P(k)$ suppression using the thermal-relic WDM cutoff (Vogel & Abazajian 2023)

$$\mathcal{T}_{\text{WDM}}(k) = [1 + (\alpha(m_{\text{WDM}}) \times k)^{2\nu}]^{-5/\nu}, \quad (2)$$

where m_{WDM} is the WDM mass, $\nu = 1.049$, and

$$\alpha(m_{\text{WDM}}) = a \left(\frac{m_{\text{WDM}}}{1 \text{ keV}} \right)^b \left(\frac{\omega_{\text{WDM}}}{0.12} \right)^\eta \left(\frac{h}{0.6736} \right)^\theta h^{-1} \text{ Mpc}, \quad (3)$$

with $a = 0.0437$, $b = -1.188$, $\theta = 2.012$, and $\eta = 0.2463$.

We consider different combinations of $P(k)$ enhancement (“bumps”) and suppression (“cutoffs”) as follows:

$$\begin{cases} \mathcal{T}_{\text{Bump+Cutoff}}(k) = \mathcal{T}_{\text{Bump}}(k) \times \mathcal{T}_{\text{WDM}}(k), & \text{Bump + Cutoff;} \\ \mathcal{T}_{\text{Cutoff}}(k) = \min [\mathcal{T}_{\text{Bump+Cutoff}}(k), 1], & \text{Cutoff;} \\ \mathcal{T}_{\text{Bump}}(k) = \max [\mathcal{T}_{\text{Bump+Cutoff}}(k), 1], & \text{Bump.} \end{cases} \quad (4)$$

For the Bump + Cutoff, Bump, and Cutoff scenarios, we generate ICs for k_0 equal to the half-mode wave number of 3 keV (22.8 Mpc⁻¹), 4 keV (32.1 Mpc⁻¹), and 5 keV (41.8 Mpc⁻¹) WDM. Figure 1 shows the resulting ratios of $P(k)$ relative to CDM; the enhanced models reach about five times the power in CDM at their respective peaks, which occur at $\approx 0.9k_0$.

We feed the Bump + Cutoff, Bump, and Cutoff transfer functions into MUSIC (Hahn & Abel 2011) to generate zoom-in ICs. Our fiducial simulations use five refinement regions, resulting in a high-resolution particle mass of $5 \times 10^4 M_\odot$; we test for convergence in Appendix A. We resimulate Halo004, and we use the COZMIC I CDM and WDM data presented at this resolution by Nadler et al. (2025a). This host recently accretes an LMC analog and merges with a Gaia-Sausage-Enceladus-analog at $z \approx 2$ (Buch et al. 2024). The highest-resolution region spans ten times the host’s 263 kpc virial radius at $z = 0$.

2.2. Zoom-in Simulations

We run zoom-in simulations using GADGET-2 (Springel et al. 2005) with Plummer-equivalent gravitational softening of 80 pc h^{-1} in the highest-resolution region. Halo catalogs and merger trees are generated using ROCKSTAR and CONSISTENT-TREES (Behroozi et al. 2013a,b). We analyze only those subhalos above 300 particles at $z = 0$, corresponding to a virial mass threshold of $M_{\text{vir}} > 1.5 \times 10^7 M_\odot$; we

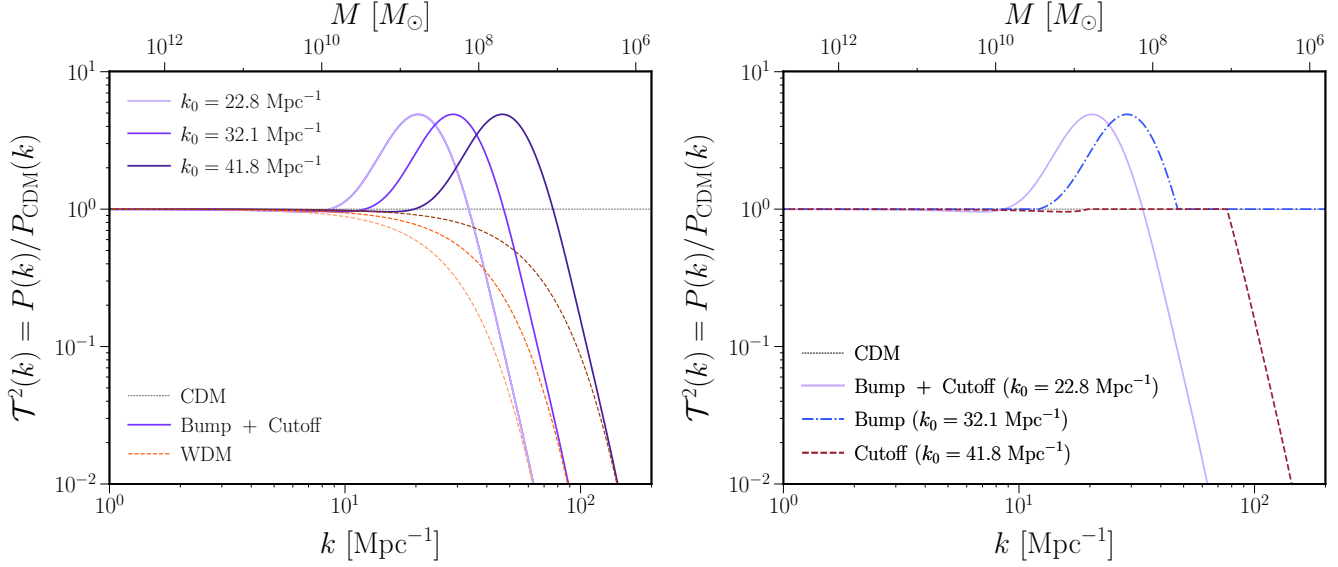


Figure 1. *Left:* Ratio of the linear matter power spectrum in our Bump + Cutoff (solid purple) and WDM (dashed orange) scenarios relative to CDM (black dotted). Models are shown with $k_0 = 22.8, 32.1$, and 41.8 Mpc^{-1} , corresponding to k_{hm} for 3, 4, and 5 keV WDM, from lightest to darkest shade. *Right:* Examples of Bump + Cutoff (solid purple), Bump (dot-dashed blue), and Cutoff (dashed red) transfer functions with different values of k_0 . In both panels, top ticks show halo masses associated with wave numbers in linear theory (Nadler et al. 2025a).

define the peak mass $M_{\text{peak}} \equiv \max(M_{\text{vir}}(z))$. Nadler et al. (2025a) showed that the fraction of spurious subhalos formed through artificial fragmentation above this mass threshold is negligible for the $P(k)$ suppression scales we simulate, so we do not remove any (sub)halos from our halo catalogs after applying this M_{vir} cut.

Host halo mass accretion histories in our zoom-ins with modified ICs are nearly identical to CDM. Figure 2 shows density projections of the CDM, Bump + Cutoff, Bump, and Cutoff simulation with $k_0 = 22.8 \text{ Mpc}^{-1}$ at $z = 0$. Subhalo abundances are visibly enhanced in the Bump + Cutoff and Bump simulations; in these scenarios, subhalos are found closer to the host center and their inner densities are noticeably higher than in CDM. We quantify these results below.

3. SUBHALO MASS FUNCTIONS

Figure 3 shows differential SHMFs in CDM and our three Bump + Cutoff simulations at $z = 0$. We restrict this figure to $M_{\text{peak}} \lesssim 10^9 M_\odot$ since all simulations contain $\lesssim 10$ subhalos, and are thus subject to large statistical uncertainties, above this threshold. We measure SHMFs down to $M_{\text{peak}} = 1.5 \times 10^7 M_\odot$, which coincides with our M_{vir} cut. Note that the CDM SHMF flattens near $M_{\text{peak}} = 1.5 \times 10^7 M_\odot$ because of this M_{vir} cut.

All Bump + Cutoff models enhance the SHMF over certain ranges of M_{peak} , but the shape and amplitude of this enhancement differ as a function of k_0 . For $k_0 = 22.8$ and 32.1 Mpc^{-1} , the enhancement is significant at high M_{peak} and weakens at lower masses, producing a feature in the SHMF that reflects the shape of $P(k)$. For example, in the $k_0 = 22.8 \text{ Mpc}^{-1}$ case, the SHMF inflects at $M_{\text{peak}} \approx 10^9 M_\odot$; this mass corresponds to $k \approx 20 \text{ Mpc}^{-1}$ in linear theory (Nadler et al. 2025a), placing it near the peak of the $k_0 = 22.8 \text{ Mpc}^{-1}$ transfer function. The

SHMF inflection occurs at lower M_{peak} for $k_0 = 32.1 \text{ Mpc}^{-1}$; this is expected because the feature in $P(k)$ occurs at a higher wave number in this case. Furthermore, SHMFs are suppressed relative to CDM at the lowest M_{peak} we consider for both $k_0 = 22.8$ and 32.1 Mpc^{-1} , since subhalos are resolved at scales where $P(k)$ is suppressed in these models.

On the other hand, the $k_0 = 41.8 \text{ Mpc}^{-1}$ SHMF is increasingly enhanced relative to CDM down to the lowest values of M_{peak} we consider. Note that $P(k)$ suppression begins at $k \approx 80 \text{ Mpc}^{-1}$ in this case, which maps to $M_{\text{peak}} \approx 10^7 M_\odot$. This mass is below our resolution limit; as a result, we do not detect the effects of $P(k)$ suppression on the SHMF for $k_0 = 41.8 \text{ Mpc}^{-1}$. This is consistent with the behavior of the SHMFs in the $k_0 = 22.8$ and 32.1 Mpc^{-1} models, which respond in a fairly localized manner to features in $P(k)$. All of these results are robust as a function of simulation resolution, as demonstrated in Appendix A.

We define the differential SHMF ratio relative to CDM,

$$f_{\text{sub}} \equiv \frac{(dN_{\text{sub}}/d \log M_{\text{peak}})_{P(k)}}{(dN_{\text{sub}}/d \log M_{\text{peak}})_{\text{CDM}}}, \quad (5)$$

where the numerator denotes either the Bump + Cutoff, Bump, or Cutoff scenario. Figure 4 shows f_{sub} for the Bump + Cutoff (solid), Bump (dot-dashed), and Cutoff (dashed) scenarios. For both $k_0 = 22.8$ and 32.1 Mpc^{-1} , we find that the SHMF is more enhanced at small M_{peak} in the Bump versus the corresponding Bump + Cutoff model, while the corresponding SHMFs are nearly identical for $k_0 = 41.8 \text{ Mpc}^{-1}$. This behavior is due to differences in the underlying transfer functions, since we resolve the effects of $P(k)$ suppression for $k_0 = 22.8$ and 32.1 Mpc^{-1} , but not for $k_0 = 41.8 \text{ Mpc}^{-1}$, in the Bump + Cutoff scenario.

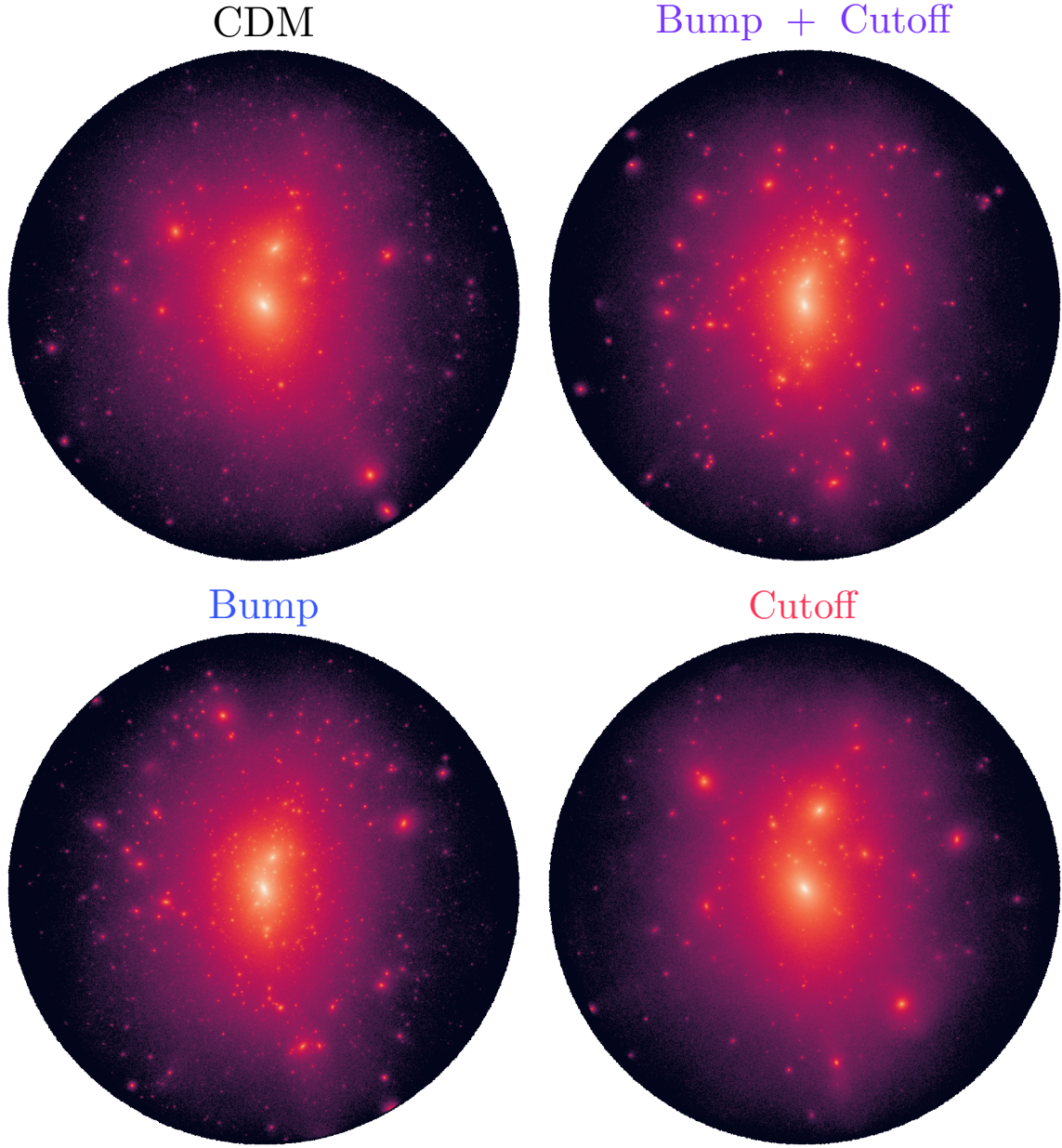


Figure 2. Projected DM density maps for our CDM (top left), Bump + Cutoff (top right), Bump (bottom left), and Cutoff (bottom right) simulations; for all non-CDM models, we show the $k_0 = 22.8 \text{ Mpc}^{-1}$ result. Each visualization is centered on the host, spans 1.5 times its virial radius, and is created using MESHOID (<https://github.com/mikegrudic/meshoid>).

As shown in Figure 4, SHMFs can differ even at scales where $P(k)$ is identical in the Bump + Cutoff and Bump scenarios. For example, f_{sub} for the $k_0 = 22.8 \text{ Mpc}^{-1}$ Bump model is larger than the corresponding Bump + Cutoff f_{sub} at $M_{\text{peak}} = 10^8 M_{\odot}$, which maps to a wave number just above the $P(k)$ peak in these models (i.e., $k > k_0$). These differences indicate efficient small-to-large scale power transfer during nonlinear structure formation (e.g., via mergers). Small-to-large scale power transfer is generally thought to be a minor effect (Little et al. 1991; Bagla et al. 2005; Bagla & Gavas 2025) but it has not been studied in a zoom-in setting before.

As expected, SHMFs are strictly suppressed relative to CDM for all models in the Cutoff scenario. Moreover, Figure 4 provides means to compare the SHMFs arising in models where the ICs are perturbed away from CDM in opposite directions: the Cutoff case captures suppression and the Bump + Cutoff case captures enhancement at the corresponding scale. We find that the amplitude of the suppression in Cutoff SHMFs is comparable to the amplitude of the enhancement in the Bump + Cutoff SHMFs, indicating that the amplitude of the effect does not depend on the sign of the perturbation to the ICs. These results are consistent with

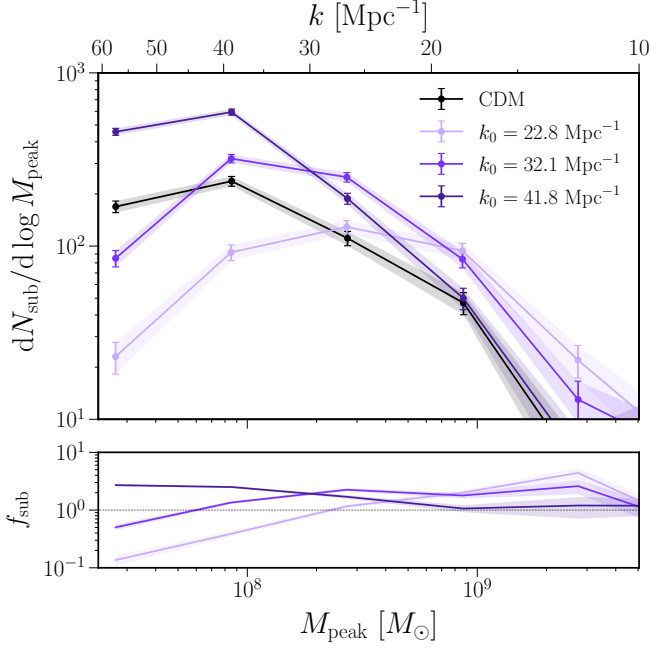


Figure 3. Differential SHMFs in CDM (black) and Bump + Cutoff (purple) models with $k_0 = 22.8, 32.1$, and 41.8 Mpc^{-1} , from lightest to darkest shade. The bottom panel shows the ratio to CDM (Equation 5). In both panels, shaded bands show 1σ Poisson uncertainties.

negligible differences in large-to-small scale power transfer among our simulations. This power transfer direction is well studied (e.g., Peebles 1980; Bagla & Padmanabhan 1997), but likely does not vary among our simulations because we fix the large-scale zoom-in environment across all runs.

In Appendix B, we show that SHMF suppression is less severe in Cutoff models compared to the corresponding WDM models. This follows because WDM $P(k)$ suppression begins at larger scales compared to the Cutoff scenario, and confirms the finding from Nadler et al. (2025a) that SHMF suppression in WDM zoom-ins is largely determined by wave numbers near the onset of the WDM transfer function suppression.

Although we simulate only one MW-like system, we expect all results throughout this section to be robust across different environments. In particular, Nadler et al. (2025a) demonstrated that $P(k)$ suppression leads to SHMF suppression relative to CDM that does not significantly vary from host to host. Nonetheless, including additional simulations would decrease the statistical uncertainty of our results.

4. PHYSICAL EFFECTS

4.1. Isolated versus Subhalo Mass Function Ratios

SHMFs in our models with $P(k)$ enhancement may deviate from CDM due to changes in the infall mass function or differences in tidal evolution. To test these explanations, we measure the ratio of the mass function for halos in the zoom-in region that are isolated at $z = 0$ relative to CDM,

$$f_{\text{iso}} \equiv \frac{(dN_{\text{iso}}/d \log M_{\text{peak}})_{P(k)}}{(dN_{\text{iso}}/d \log M_{\text{peak}})_{\text{CDM}}} \quad (6)$$

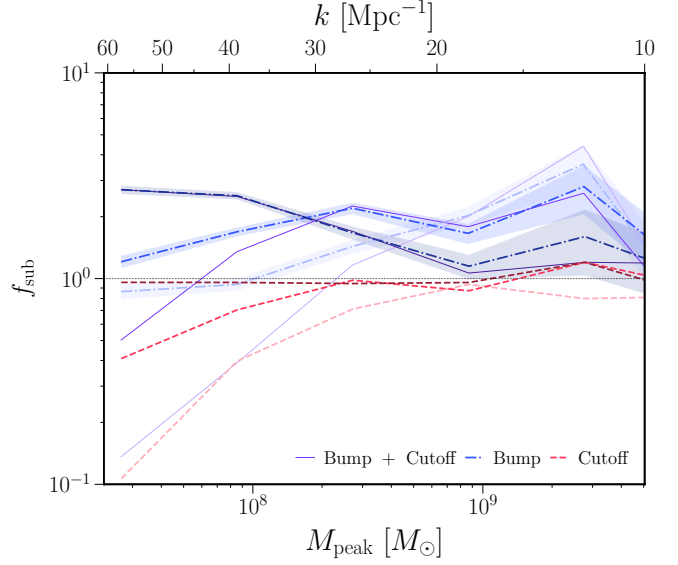


Figure 4. Ratio of the differential SHMF relative to CDM (Equation 5). Results are shown for Bump + Cutoff (solid purple), Bump (dot-dashed blue), and Cutoff (dashed red) models with $k_0 = 22.8, 32.1$, and 41.8 Mpc^{-1} , from lightest to darkest shade. Shaded bands show 1σ Poisson uncertainties for the Bump results.

We restrict our isolated halo sample to objects that have never been a subhalo of a larger host, which excludes splashback systems that have previously been stripped, and we consider only objects within 2.63 Mpc of the host center (corresponding to ten times the virial radius of the MW host) at $z = 0$. Figure 5 shows $f_{\text{sub}}/f_{\text{iso}}$ in our Bump + Cutoff and Bump models. We omit the Cutoff models since the $k_0 = 22.8 \text{ Mpc}^{-1}$ case behaves similarly to the corresponding Bump + Cutoff model at low M_{peak} , while the results for higher- k_0 models are consistent with unity at all M_{peak} that we consider.

To first order, Figure 5 shows that changes to the SHMF are determined by changes to the isolated HMF. In particular, $f_{\text{sub}}/f_{\text{iso}}$ differs from unity by at most $\approx 25\%$ in all models, except at the high- M_{peak} end, which we discuss below. Although this difference is significant given the statistical errors on our SHMF measurements, it is small relative to the variations in f_{sub} shown in the bottom panel of Figure 3.

The behavior of $f_{\text{sub}}/f_{\text{iso}}$ for the $k_0 = 22.8 \text{ Mpc}^{-1}$ Bump + Cutoff model is particularly informative. In this model, both $P(k)$ enhancement and suppression are well resolved. The scale of the $P(k)$ enhancement corresponds to the highest M_{peak} shown in Figure 5, while the $P(k)$ suppression scale corresponds to the lowest M_{peak} we plot. At high M_{peak} , $f_{\text{sub}}/f_{\text{iso}}$ becomes much larger than unity, indicating that subhalos formed from modes near the $P(k)$ peak are more resilient to tidal disruption than CDM subhalos with similar values of M_{peak} , and vice versa for subhalos with low M_{peak} .⁴

⁴ Note that M_{peak} itself does not significantly differ among matched (sub)halos in the different simulations.

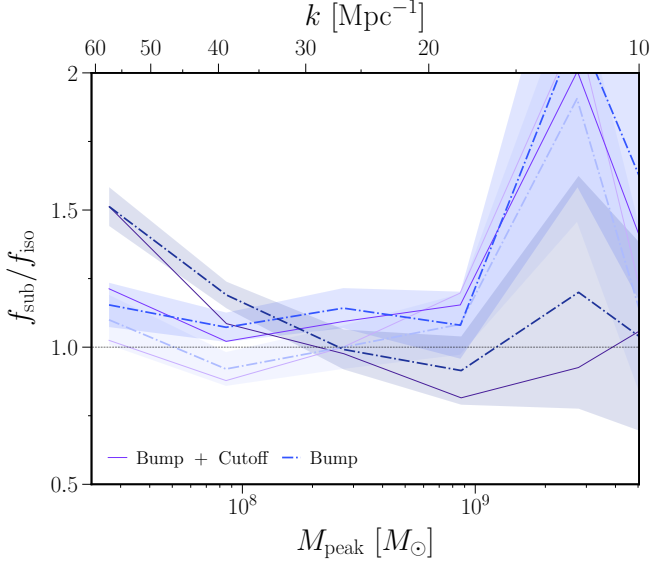


Figure 5. Ratio of the differential SHMF in our models with $P(k)$ enhancement relative to CDM divided by the corresponding ratio for isolated halos (Equation 6). Results are shown for Bump + Cutoff (solid purple) and Bump (dot-dashed blue) models with $k_0 = 22.8, 32.1, \text{ and } 41.8 \text{ Mpc}^{-1}$, from lightest to darkest shade. Shaded bands show 1σ Poisson uncertainties for the Bump results. The differences in subhalo vs. isolated halo abundances shown here are small compared to the differences in SHMFs relative to CDM that are imprinted by $P(k)$ (see Figure 4).

This is consistent with the effects of $P(k)$ on subhalo concentrations demonstrated in Section 4.3. Furthermore, the differences between the Bump + Cutoff and Bump results are consistent with this explanation. For example, at low M_{peak} , $f_{\text{sub}}/f_{\text{iso}}$ is not significantly suppressed in the Bump model since it does not have a $P(k)$ cutoff. Meanwhile, the $P(k)$ peak in the $k_0 = 41.8 \text{ Mpc}^{-1}$ case corresponds to the lowest M_{peak} we plot, which explains why $f_{\text{sub}}/f_{\text{iso}}$ rises toward low M_{peak} in this case, as does f_{sub} itself.

4.2. Subhalo Radial Distribution

The changes to the SHMF in our models with $P(k)$ enhancement have implications for the subhalo radial distribution. In particular, subhalos with higher infall masses sink to the host center more quickly due to dynamical friction, resulting in a more concentrated radial distribution (e.g., Nadler et al. 2023). Thus, we expect a more centrally concentrated radial distribution for models that enhance the SHMF relative to CDM at high M_{peak} , and a less centrally concentrated radial distribution for models that enhance the SHMF at low M_{peak} . Conversely, we expect models that suppress the SHMF at low M_{peak} to yield a more centrally concentrated radial distribution (e.g., Lovell et al. 2021).

Figure 6 shows normalized radial distributions of subhalos with $1.5 \times 10^7 M_\odot < M_{\text{peak}} < 5 \times 10^8 M_\odot$ in CDM and Bump + Cutoff models; the lower limit corresponds to our resolution cut. We illustrate the mass dependence of the ra-

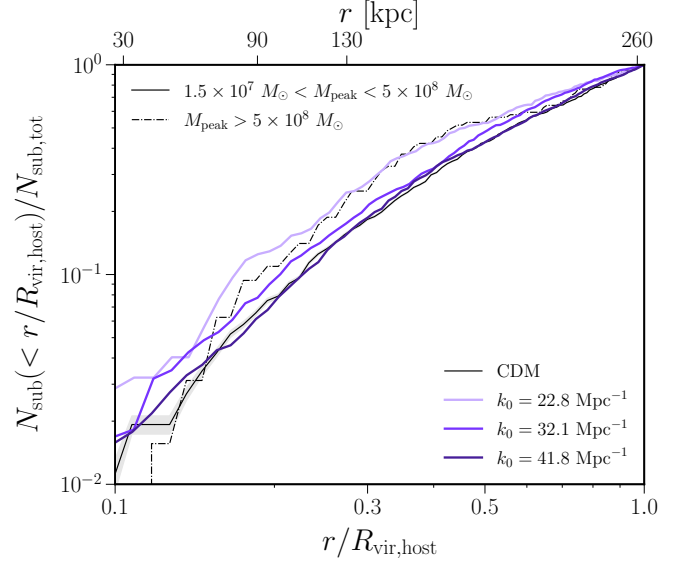


Figure 6. Normalized radial distribution of subhalos with $1.5 \times 10^7 M_\odot < M_{\text{peak}} < 5 \times 10^8 M_\odot$ in CDM (black) and Bump + Cutoff models (purple) with $k_0 = 22.8, 32.1, \text{ and } 41.8 \text{ Mpc}^{-1}$, from lightest to darkest shade. The dot-dashed black line shows the CDM result for subhalos with $M_{\text{peak}} > 5 \times 10^8 M_\odot$. The shaded gray band shows 1σ Poisson uncertainty for the CDM result. Note that the host halo’s virial radius is $R_{\text{vir,host}} = 263 \text{ kpc}$ in all simulations. Models that enhance $P(k)$ at higher M_{peak} yield more centrally-concentrated radial distributions.

dial distribution by overplotting the CDM radial distribution for subhalos with $M_{\text{peak}} > 5 \times 10^8 M_\odot$.⁵ As expected, higher- M_{peak} subhalos are significantly more centrally concentrated.

The Bump + Cutoff radial distributions become more centrally concentrated as k_0 decreases; for example, the $k_0 = 22.8 \text{ Mpc}^{-1}$ result for $1.5 \times 10^7 M_\odot < M_{\text{peak}} < 5 \times 10^8 M_\odot$ is similar to the CDM result for $M_{\text{peak}} > 5 \times 10^8 M_\odot$. This follows because the Bump + Cutoff models both enhance the SHMF at high M_{peak} and suppress it at low M_{peak} , compounding the dynamical friction effect described above, and the amplitude of these effects grows as k_0 decreases. We have checked that the individual effects of $P(k)$ enhancement (in the Bump scenario) and suppression (in the Cutoff scenario) scenario change the radial distribution much less than in the Bump + Cutoff scenario. This is consistent with the finding in Nadler et al. (2025a) that WDM radial distributions do not significantly differ from CDM given the cutoff scales we simulate and the subhalo masses we resolve.

Finally, we note that matched subhalos are found closer to the host center in models with $P(k)$ enhancement, and farther in models with $P(k)$ suppression, relative to CDM. Figure 2 clearly illustrates this for the LMC analog—the largest sub-

⁵ This $5 \times 10^8 M_\odot$ threshold is chosen to ensure that there are enough high-mass subhalos to reliably measure the radial distribution when splitting the population in this way.

halo directly above the host in each panel—in the Bump + Cutoff, Bump, and Cutoff scenarios. These LMC analogs’ orbits are very similar before infall. In the Bump + Cutoff and Bump scenarios, they sink to the host center more quickly after crossing into the MW host’s virial radius. This could be due to differences in the mass loss rates or in the strength of dynamical friction across the scenarios; we leave a study of these effects to future work.

4.3. Subhalo Mass–Concentration Relation

We expect (sub)halo concentrations to increase relative to CDM in scenarios with $P(k)$ enhancement, and decrease in scenarios with $P(k)$ suppression. We quantify this effect using subhalos with ≥ 2000 particles, or $M_{\text{vir}} > 10^8 M_\odot$, using the effective concentration (Yang et al. 2023)

$$c_{\text{eff}} = \frac{R_{\text{vir}}}{R_{\text{max}}/2.126}, \quad (7)$$

where R_{vir} is the virial radius and R_{max} is the radius from the center of a given subhalo at which the maximum circular velocity V_{max} is achieved. We use c_{eff} because it reduces to the virial concentration for Navarro–Frenk–White (NFW; Navarro et al. 1997) halos while flexibly capturing non-NFW profiles resulting from nonstandard ICs and/or tidal stripping.

Figure 7 shows the $c_{\text{eff}}-M_{\text{peak}}$ relation for subhalos in our CDM and $k_0 = 22.8$ and 41.8 Mpc^{-1} Bump simulations. Subhalos in the Bump simulations are generally more concentrated than their CDM counterparts, reaching $c_{\text{eff}} \approx 50$, whereas the most concentrated CDM subhalos have $c_{\text{eff}} \approx 30$. This enhancement is most pronounced at $M_{\text{peak}} \approx 10^{9.5} M_\odot$ in the $k_0 = 22.8 \text{ Mpc}^{-1}$ case and at $M_{\text{peak}} \approx 10^8 M_\odot$ in the $k_0 = 41.8 \text{ Mpc}^{-1}$. This reflects the shift of the peak in the underlying transfer function between the two scenarios and aligns with the mass scales where the respective SHMFs are most strongly enhanced relative to CDM. The concentration distribution for the $k_0 = 32.1 \text{ Mpc}^{-1}$ model peaks at intermediate masses, as expected.

We find that this behavior is similar in the Bump + Cutoff scenario, although the high- c_{eff} region of Figure 7 is somewhat less populated in these models. Meanwhile, subhalos in the Cutoff runs systematically shift toward smaller c_{eff} than CDM due to $P(k)$ suppression, consistent with the results in Nadler et al. (2025b) for simulations of self-interacting dark matter models with $P(k)$ suppression but without late-time scattering. Across all $P(k)$ scenarios and values of k_0 , we find that differences in the $c_{\text{eff}}-M_{\text{peak}}$ relation relative to CDM are similar when considering isolated halos rather than subhalos.

The response of the mass–concentration relation to $P(k)$ enhancement and/or suppression can thus be used to place constraints that are complementary to—but not entirely independent of—constraints from (sub)halo abundances. This idea has recently been used to constrain cosmologies where $P(k)$ is affected over a range of scales using dwarf galaxy stellar velocity dispersions (Esteban et al. 2024; Dekker et al. 2022) and strong-lensing substructure (Gilman et al. 2022). It will be interesting to revisit this signature to probe models with localized features in $P(k)$.

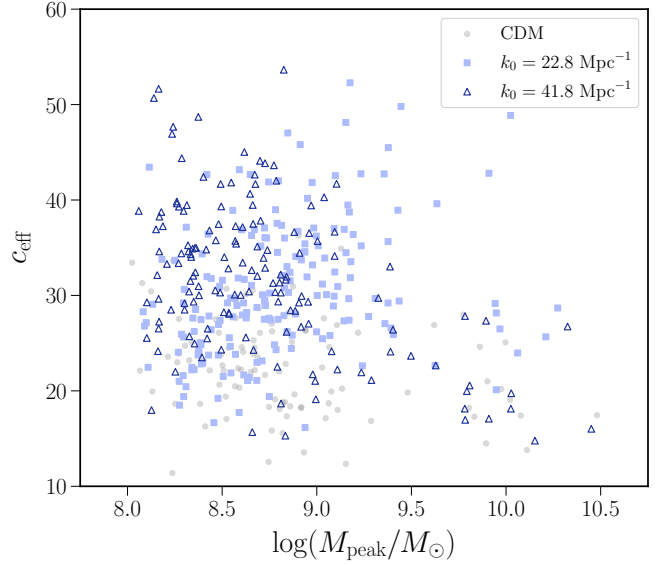


Figure 7. Effective concentration (Equation 7) versus peak virial mass for subhalos with $M_{\text{vir}} > 10^8 M_\odot$ in our CDM simulation (gray circles), along with our $k_0 = 22.8 \text{ Mpc}^{-1}$ (light blue squares) and 41.8 Mpc^{-1} (dark blue unfilled triangles) Bump simulations. Subhalo concentrations are amplified relative to CDM in models with $P(k)$ enhancement.

5. SUMMARY AND DISCUSSION

5.1. Summary

We have presented new zoom-in simulations of a MW analog with initial conditions featuring linear matter power spectrum enhancement and/or suppression. We highlight the following key results:

- The subhalo mass function reflects the shape of $P(k)$, including both its enhancement and suppression when they are present (Figures 3 and 4);
- Changes to the SHMF relative to CDM are mainly imprinted at infall, rather than during tidal evolution (Figure 5);
- $P(k)$ enhancement yields more centrally-concentrated subhalo radial distributions (Figure 6).

These results are consistent with previous simulations that include Gaussian $P(k)$ enhancement, but probe a different range of spatial and temporal scales. In particular, Tkachev et al. (2024a,b), Pilipenko et al. (2024), and Eroshenko et al. (2024) found that a Gaussian $P(k)$ bump leads to HMF enhancement relative to CDM at high redshifts. Figures 3 and 4 demonstrate that this enhancement persists in the $z = 0$ SHMF. This finding is not guaranteed from the high- z results, since mode coupling tends to erase power spectrum features over time. These previous studies also showed that central densities of halos in the Gaussian enhancement scenarios are increased relative to CDM, consistent with Figure 7.

5.2. Implications for Semi-analytic Models

The relatively tight correspondence that we find between $P(k)$ and SHMF features has important consequences for semi-analytic structure formation models. In scenarios with $P(k)$ suppression, extended Press–Schechter (ePS) window functions that truncate sharply as a function of wave number predict mass functions more accurately compared to sharp real-space filters, which work well in CDM (e.g., Benson et al. 2013; Leo et al. 2018). This situation is relatively unexplored for models with $P(k)$ enhancement, but our results generally suggest that the mapping from $P(k)$ to mass functions remains relatively sharp in these scenarios, including when $P(k)$ suppression is also present.

We note that ePS models can make surprising predictions in scenarios with $P(k)$ enhancement. For example, Balaji et al. (2024) predicted that strict $P(k)$ enhancement relative to CDM in a supermassive black hole model can lead to SHMF *suppression* at masses that correspond to scales smaller than the $P(k)$ enhancement ($k > k_0$). Mathematically, this follows from combining a Gaussian $P(k)$ enhancement with an exponential k -space ePS window function. Physically, these authors reasoned that high-mass halos formed from modes near the transfer function peak collapse earlier than in CDM, preventing the formation of smaller halos within these systems. We do not find evidence of this effect in our Bump simulations down to the smallest values of M_{peak} we resolve, as shown by Figure 4. Higher-resolution zoom-in simulations would be needed to study whether this effect is relevant at lower values of M_{peak} .

5.3. Future Work

$P(k)$ enhancement and suppression can arise in many non-standard inflation and DM models. For example, features in the inflaton potential imprint oscillations in the primordial power spectrum, which can translate to $P(k)$ enhancements that qualitatively resemble the models we simulate (Adams et al. 2001). Meanwhile, axions produced with a large misalignment angle yield $P(k)$ that resemble our Bump + Cutoff transfer function model (Arvanitaki et al. 2020). We expect that our simulation results can be mapped to these scenarios. The opposite behavior—i.e., a $P(k)$ cutoff followed on smaller scales by an enhancement—can arise in ultralight dark matter models due to a combination of free-streaming and white-noise effects (Amin & Mirbabayi 2024). These scenarios will be interesting to simulate in our framework.

Additional simulations will be needed to assess the effects of mode coupling for models that affect $P(k)$ over a wider range of wave numbers, including cosmologies with a running spectral index (e.g., Garrison-Kimmel et al. 2014; Wu et al. 2025; Colazo et al. 2025). This is a timely direction for future work because these models have recently been constrained using small-scale structure observables (Gilman et al. 2022; Esteban et al. 2024; Dekker & Kravtsov 2025).

5.4. Outlook

Our results underscore the importance of modeling the mapping from $P(k)$ to small-scale DM structure using cosmological simulations. In particular, (sub)halos populations sourced from density perturbations over a given range of wave numbers are sensitive to the shape of $P(k)$ due to non-linear mode coupling during structure formation. Thus, our results affirm optimism that $P(k)$ reconstruction is feasible on small scales, following classic techniques developed for large-scale structure observables (e.g., Weinberg 1992).

The simulations presented in this work will help enable $P(k)$ reconstruction using the Milky Way satellite population. This is an exciting direction given upcoming data from the Vera C. Rubin Observatory, which is expected to significantly increase the number of detected satellites (Tsiane et al. 2025) and improve DM constraints (Bechtol et al. 2019; Drlica-Wagner et al. 2019). In particular, Nadler et al. (2024) showed that SHMF enhancement can be probed using upcoming satellite luminosity function observations; in turn, these constraints can be mapped to $P(k)$. Complementary data including stellar velocity dispersion measurements will likely further boost this sensitivity, although hydrodynamic simulations in enhanced $P(k)$ scenarios will be needed to assess this precisely. More generally, deriving robust $P(k)$ constraints using DM substructure will require the development of a fast, flexible, and general forward modeling framework, which will be the focus of future studies.

ACKNOWLEDGMENTS

This material is based upon work supported by the National Science Foundation under Grant No. 2509561 (E.O.N. and A.B.) and No. 2407380 (V.G.). Any opinions, findings, and conclusions or recommendations expressed in this material are those of the author(s) and do not necessarily reflect the views of the NSF. This research was supported in part by grant NSF PHY-2309135 to the Kavli Institute for Theoretical Physics (KITP). V.G. additionally acknowledges the support from NASA through the Astrophysics Theory Program, Award Number 21-ATP21-0135, from the National Science Foundation (NSF) CAREER Grant No. PHY-2239205, and from the Research Corporation for Science Advancement through the Cottrell Scholars program.

The computations presented here were conducted through Carnegie’s partnership in the Resnick High Performance Computing Center, a facility supported by Resnick Sustainability Institute at Caltech. This work used data from COZMIC I, which is available at 10.5281/zenodo.14649137. This work used data from the Milky Way-est suite of simulations, hosted at <https://web.stanford.edu/group/gfc/gfcsims/>, which was supported by the Kavli Institute for Particle Astrophysics and Cosmology at Stanford, SLAC National Accelerator Laboratory, and the U.S. DoE under contract number DE-AC02-76SF00515 to SLAC.

Software: CONSISTENT-TREES (Behroozi et al. 2013b), HELPERS (bitbucket.org/yymao/helpers/src/master/), JUPYTER (jupyter.org), MATPLOTLIB (Hunter 2007), NUMPY (van der Walt et al. 2011), PYNBODY (Pontzen et al. 2013), ROCKSTAR (Behroozi et al. 2013a), SCIPY (Jones et al. 2001), SEABORN (seaborn.pydata.org).

REFERENCES

- Achúcarro, A., Biagetti, M., Braglia, M., et al. 2022, [arXiv e-prints](#), [arXiv:2203.08128](#)
- Adams, J., Cresswell, B., & Easther, R. 2001, *PhRvD*, **64**, 123514
- Allahverdi, R., Amin, M. A., Berlin, A., et al. 2021, *The Open Journal of Astrophysics*, **4**, 1
- Amin, M. A. & Mirbabayi, M. 2024, *PhRvL*, **132**, 221004
- An, R., Nadler, E. O., Benson, A., & Gluscevic, V. 2025, *ApJ*, **986**, 128
- Arbey, A. & Mahmoudi, F. 2021, *Progress in Particle and Nuclear Physics*, **119**, 103865
- Arvanitaki, A., Dimopoulos, S., Galanis, M., et al. 2020, *PhRvD*, **101**, 083014
- Bagla, J. S. & Gavas, S. 2025, *Journal of Astrophysics and Astronomy*, **46**, 33
- Bagla, J. S. & Padmanabhan, T. 1997, *MNRAS*, **286**, 1023
- Bagla, J. S., Prasad, J., & Ray, S. 2005, *MNRAS*, **360**, 194
- Balaji, S., Ando, S., Fairbairn, M., Hiroshima, N., & Ishiwata, K. 2024, [arXiv e-prints](#), [arXiv:2408.11098](#)
- Bechtol, K., Drlica-Wagner, A., Abazajian, K. N., et al. 2019, *BAAS*, **51**, 207
- Bechtol, K., Birrer, S., Cyr-Racine, F.-Y., et al. 2022, [arXiv e-prints](#), [arXiv:2203.07354](#)
- Behroozi, P. S., Wechsler, R. H., & Wu, H.-Y. 2013a, *ApJ*, **762**, 109
- Behroozi, P. S., Wechsler, R. H., Wu, H.-Y., et al. 2013b, *ApJ*, **763**, 18
- Benson, A. J. & Du, X. 2022, *MNRAS*, **517**, 1398
- Benson, A. J., Farahi, A., Cole, S., et al. 2013, *MNRAS*, **428**, 1774
- Bryan, G. L. & Norman, M. L. 1998, *ApJ*, **495**, 80
- Buch, D., Nadler, E. O., Wechsler, R. H., & Mao, Y.-Y. 2024, *ApJ*, **971**, 79
- Buschmann, M., Foster, J. W., & Safdi, B. R. 2020, *PhRvL*, **124**, 161103
- Colazo, P., Padilla, N., & Stasyszyn, F. 2025, [arXiv e-prints](#), [arXiv:2505.23896](#)
- Dekker, A., Ando, S., Correa, C. A., & Ng, K. C. Y. 2022, *PhRvD*, **106**, 123026
- Dekker, A. & Kravtsov, A. 2025, *PhRvD*, **111**, 063516
- Delos, M. S. & White, S. D. M. 2023, *MNRAS*, **518**, 3509
- Drlica-Wagner, A., Mao, Y.-Y., Adhikari, S., et al. 2019, [arXiv e-prints](#), [arXiv:1902.01055](#)
- Erickcek, A. L. & Sigurdson, K. 2011, *PhRvD*, **84**, 083503
- Eroshenko, Y. N., Lukash, V. N., Mikheeva, E. V., Pilipenko, S. V., & Tkachev, M. V. 2024, *Soviet Journal of Experimental and Theoretical Physics Letters*, **120**, 83
- Errani, R. & Navarro, J. F. 2021, *MNRAS*, **505**, 18
- Esteban, I., Peter, A. H. G., & Kim, S. Y. 2024, *PhRvD*, **110**, 123013
- Garrison-Kimmel, S., Horiuchi, S., Abazajian, K. N., Bullock, J. S., & Kaplinghat, M. 2014, *MNRAS*, **444**, 961
- Gilman, D., Benson, A., Bovy, J., et al. 2022, *MNRAS*, **512**, 3163
- Gorghetto, M., Hardy, E., & Villadoro, G. 2021, *SciPost Physics*, **10**, 050
- Graham, P. W., Mardon, J., & Rajendran, S. 2016, *PhRvD*, **93**, 103520
- Hahn, O. & Abel, T. 2011, *MNRAS*, **415**, 2101
- Hinshaw, G., Larson, D., Komatsu, E., et al. 2013, *ApJS*, **208**, 19
- Hunter, J. D. 2007, *Computing in Science Engineering*, **9**, 90
- Jones, E., Oliphant, T., Peterson, P., et al. 2001, SciPy: Open source scientific tools for Python, [Online; [scipy.org](#)]
- Leo, M., Baugh, C. M., Li, B., & Pascoli, S. 2018, *JCAP*, **2018**, 010
- Little, B., Weinberg, D. H., & Park, C. 1991, *MNRAS*, **253**, 295
- Lovell, M. R., Cautun, M., Frenk, C. S., Hellwing, W. A., & Newton, O. 2021, *MNRAS*, **507**, 4826
- Nadler, E. O., An, R., Gluscevic, V., Benson, A., & Du, X. 2025a, *ApJ*, **986**, 127
- Nadler, E. O., An, R., Yang, D., et al. 2025b, *ApJ*, **986**, 129
- Nadler, E. O., Gluscevic, V., Driskell, T., et al. 2024, *ApJ*, **967**, 61
- Nadler, E. O., Mansfield, P., Wang, Y., et al. 2023, *ApJ*, **945**, 159
- Navarro, J. F., Frenk, C. S., & White, S. D. M. 1997, *ApJ*, **490**, 493
- Palma, G. A., Sypas, S., & Zenteno, C. 2020, *PhRvL*, **125**, 121301
- Pavičević, M., Iršič, V., Viel, M., et al. 2025, [arXiv e-prints](#), [arXiv:2501.06299](#)
- Peebles, P. J. E. 1980, The large-scale structure of the universe
- Pilipenko, S. V., Drozdov, S. A., Tkachev, M. V., & Doroshkevich, A. G. 2024, [arXiv e-prints](#), [arXiv:2404.17803](#)
- Pontzen, A., Roškar, R., Stinson, G., & Woods, R. 2013, pynbody: N-Body/SPH analysis for python, Astrophysics Source Code Library, record ascl:1305.002
- Power, C., Navarro, J. F., Jenkins, A., et al. 2003, *MNRAS*, **338**, 14
- Springel, V., White, S. D. M., Jenkins, A., et al. 2005, *Nature*, **435**, 629
- Tkachev, M. V., Pilipenko, S. V., Mikheeva, E. V., & Lukash, V. N. 2024a, *MNRAS*, **527**, 1381
- Tkachev, M. V., Pilipenko, S. V., Mikheeva, E. V., & Lukash, V. N. 2024b, *PhRvD*, **110**, 083530
- Tsiane, K., Mau, S., Drlica-Wagner, A., et al. 2025, *The Open Journal of Astrophysics*, **8**
- van den Bosch, F. C., Ogiya, G., Hahn, O., & Burkert, A. 2018, *MNRAS*, **474**, 3043
- van der Walt, S., Colbert, S. C., & Varoquaux, G. 2011, *Computing in Science Engineering*, **13**, 22
- Vogel, C. M. & Abazajian, K. N. 2023, *PhRvD*, **108**, 043520
- Weinberg, D. H. 1992, *MNRAS*, **254**, 315
- Wu, J., Chan, T. K., & Forouhar Moreno, V. J. 2025, *PhRvD*, **112**, 023512
- Yang, D., Nadler, E. O., & Yu, H.-B. 2023, *ApJ*, **949**, 67

APPENDIX

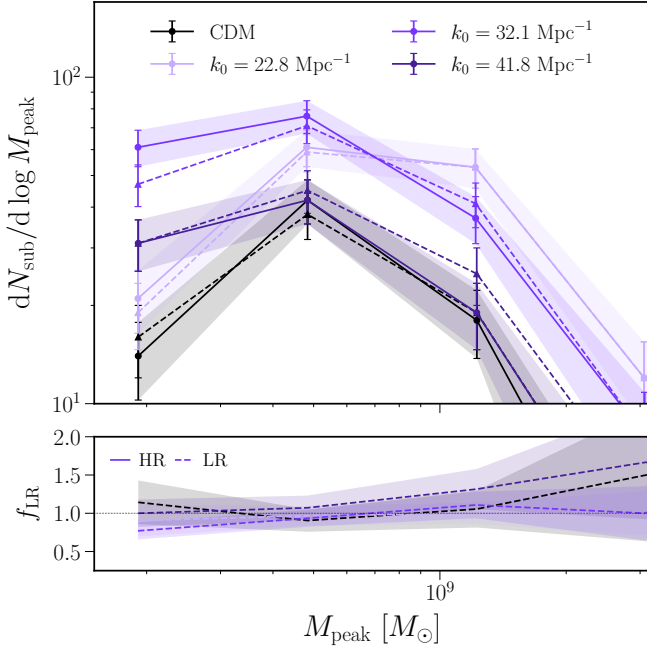


Figure 8. Same as Figure 3, but comparing the differential SHMF in our LR (dashed) vs. HR (solid) simulations. We show CDM (black) and Bump + Cutoff (purple) models with $k_0 = 22.8, 32.1$, and 41.8 Mpc^{-1} , from lightest to darkest shade. The bottom panel shows the SHMF ratio between each LR/HR pair. In both panels, shaded bands show 1σ Poisson uncertainties for the HR results.

A. CONVERGENCE TESTS

To test for convergence, we resimulate all models using one fewer MUSIC refinement region when generating ICs, which results in a high-resolution DM mass of $4 \times 10^5 M_\odot$. For these low-resolution (LR) runs, we use a softening of $\epsilon = 170 \text{ pc } h^{-1}$. Large-scale features of the simulations, including the host halo mass accretion history, are nearly identical between resolution levels. In the following analyses, we apply a $M_{\text{vir}} > 1.2 \times 10^8 M_\odot$ cut to the resulting subhalo populations, which corresponds to 300 particles in the LR runs.

The top panel of Figure 8 compares the differential SHMF in the CDM and Bump + Cutoff LR runs to the high-resolution (HR) simulations we used in our main analysis. In the bottom panel, we further compare the runs using

$$f_{\text{LR}} \equiv \frac{(dN_{\text{sub,LR}}/d \log M_{\text{peak}})_{P(k)}}{(dN_{\text{sub,HR}}/d \log M_{\text{peak}})_{P(k)}}. \quad (\text{A1})$$

All f_{LR} measurements are consistent with unity given the Poisson uncertainties on our LR SHMFs. Thus, our SHMF measurements are converged down to a 300-particle limit, lending confidence to our main results. We obtain similar levels of agreement for the Bump and Cutoff scenarios.

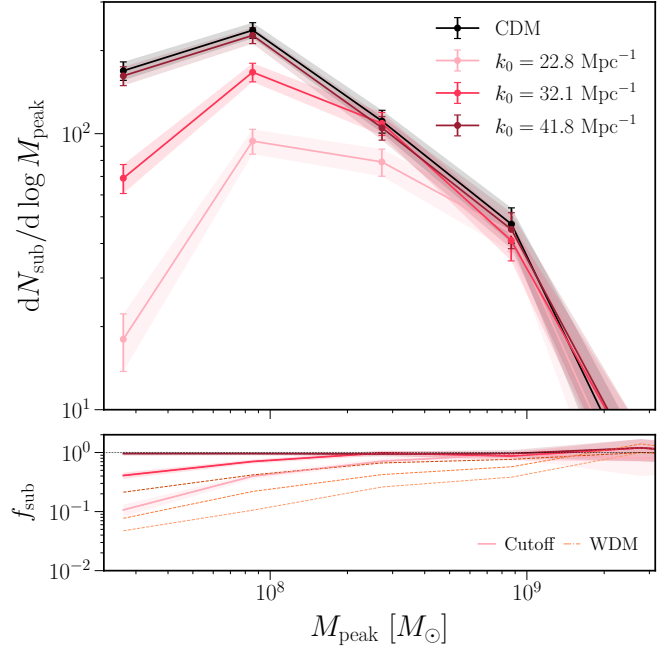


Figure 9. Same as Figure 3, but comparing the differential SHMF in CDM (black) to Cutoff (red) models with $k_0 = 22.8, 32.1$, and 41.8 Mpc^{-1} , from lightest to darkest shade. The bottom panel shows the ratio of the SHMF to CDM in the Cutoff (solid red) and WDM (dashed orange) scenarios. In both panels, shaded bands show 1σ Poisson uncertainties.

B. SHMF COMPARISON FOR CUTOFF VERSUS WDM SCENARIOS

Figure 9 compares the SHMF in the Cutoff and WDM scenarios. As discussed in Section 3, WDM SHMFs are more suppressed than the corresponding Cutoff SHMFs because transfer function suppression begins at larger scales in WDM. This is consistent with the comparisons between DM models with different transfer function shapes and suppression scales in Nadler et al. (2025a).